High-speed AFM height spectroscopy reveals µs-dynamics of unlabeled biomolecules

George R Heath[1,2] and Simon Scheuring[1,2,*]

[1] Weill Cornell Medicine, Department of Anesthesiology, 1300 York Avenue, New York, NY-10065, USA.
[2] Weill Cornell Medicine, Department of Physiology and Biophysics, 1300 York Avenue, New York, NY-10065, USA.
* Correspondence to: sis2019@med.cornell.edu

Abstract:

Dynamics are fundamental to the functions of biomolecules and can occur on a wide range of time- and length-scales. Here we develop and apply high-speed AFM height spectroscopy (HS-AFM-HS), a technique whereby we monitor the sensing of a HS-AFM tip at a fixed position to directly detect the motions of unlabeled molecules underneath. This gives Angstrom spatial and microsecond temporal resolutions. In conjunction with HS-AFM imaging modes to precisely locate areas of interest, HS-AFM-HS measures simultaneously surface concentrations, diffusion coefficients and oligomer sizes of annexin-V on model membranes to decipher key kinetics allowing us to describe the entire annexin-V membrane-association and self-assembly process in great detail and quantitatively. This work displays how HS-AFM-HS can assess the dynamics of unlabeled bio-molecules over several orders of magnitude and separate the various dynamic components spatiotemporally.

Introduction:

Developing a full picture of how biomolecules function requires an understanding of the intricate relationships between structure and dynamics. For molecules in isolation such as single proteins, these dynamics generally occur as conformational changes. For molecules that act in complexes, the dynamics are dependent on diffusion and partner interaction. These dynamic processes are of course not mutually exclusive, but occur in different spatiotemporal regimes. For membrane proteins these dynamics are crucial as they allow the cell to reorganize proteins in space and time, to form temporal functional units for a particular biochemical function or to regulate the function of the membrane protein itself.[1,2]

Biomolecule dynamics occur over a range of length and timescales. Local flexibility, which generally concerns side chain rotations, bond vibrations and loop motions, happens over the femtosecond to nanosecond time range. Whereas collective motions of groups of atoms, loops and domains, typically occur on timescales of the microsecond or longer. Such collective motions are at the basis of most important biomolecular functions including conformational changes between functional states of proteins, the working of molecular machines, enzyme catalysis, protein folding and protein-protein interactions, though the later phenomena can extend into the millisecond to second time range depending on the process or the origin of the molecules under investigation.[3] Thus, developing techniques to directly access structural changes from the microsecond to second timescales is key to understanding the behavior of biomolecules.

X-ray crystallography and electron microscopy (EM), are most powerful techniques to study biomolecular structures,[4,5] whilst able to provide unparalleled spatial resolution, the structures obtained from these methods are limited by ensemble averaging and static snapshots of fixed conformations. Consequently, dynamics must be inferred, missing vital information describing how the biomolecules truly function in native conditions, such as their fluctuations, rates, intermediate states and statistical distributions. Nuclear magnetic resonance (NMR) spectroscopy provides both structural and dynamic information on biomolecules but is currently suited to smaller soluble proteins and picosecond to nanosecond timescale dynamics of specific sites.[6]

A number of different light microscopy techniques can observe dynamics of single molecules. However, despite significant improvements in the localization resolution with methods such as stimulated emission depletion microscopy (STED)[7] and stochastic optical reconstruction microscopy (STORM),[8,9] the imaging resolution is not able to go below ~20nm.[10] Such resolution does not allow protein-protein interactions to be directly observed, nor does it enable structural features or dynamics to be assessed. A method that is sensitive to less than 10nm with a time resolution of typically ~10 milliseconds is fluorescence resonance energy transfer (FRET). The spatial resolution of FRET is dependent on the Förster radius of the pair of fluorescent molecules between which energy is transferred.[11] FRET is sensitive to distance changes as small as 0.3nm in the 3–10nm inter-dye distance range.[12] However, reducing the Förster radius also reduces the technique's sensitivity range, limiting it to site specific interactions over specific spatial windows. A technique that can access nanosecond timescales is fluorescence correlation spectroscopy (FCS).[13] By measuring intensity fluctuations as fluorescent molecules diffuse in and out of a detection volume, FCS can determine concentrations, mobility and interactions of labeled molecules. Spatially however

72 FCS is limited by the diffraction limit to hundreds of nm resolutions and can suffer
73 from poor autocorrelation signal-to-noise ratio at high molecular densities. The spatial
74 resolution can be improved to as low as 30nm using a combination of methods such
75 as FCS-STED, however this is often at the expense of lower temporal resolution.[14]
76 Similarly the temporal resolution of FRET has been improved to sub-millisecond time
77 scales using diffusion-based FRET to detect one molecule at a time as it freely
78 diffuses in solution. However, in this condition the length that a single molecule can
79 be measured is greatly reduced to ~10ms.[15]

80 Whilst many of these techniques can provide valuable insight into
81 biomolecular processes, few can simultaneously provide structural and dynamical
82 information of single molecules on microsecond timescales, and none can provide
83 microsecond time resolution over seconds or minutes of observation. Additionally,
84 these techniques require labeling of molecules that can modify the very dynamics of
85 interest. High-speed AFM (HS-AFM) offers a label-free technique that has
86 submolecular imaging resolution with high spatiotemporal resolution, ~1nm lateral,
87 ~0.1nm vertical and ~100ms temporal resolution. Although HS-AFM proves to be a
88 valuable tool in understanding the function and behavior of many proteins at the
89 single molecule level[16,17,18] there are many molecular processes that are too fast to
90 be resolved in imaging mode.[19,20] Progress in developing faster HS-AFM is ongoing
91 but it may be unlikely to reach sub-millisecond imaging resolution in the near future.

92 Here, inspired by fluorescence spectroscopy, we develop and apply HS-AFM
93 height spectroscopy (HS-AFM-HS), a technique whereby we hold the AFM tip at a
94 fixed x-y position and monitor the height fluctuations under the tip in z-direction with
95 Angstrom spatial and 10µs temporal resolution. We demonstrate how this technique
96 can be used to simultaneously measure surface concentrations, diffusion rates and
97 oligomer sizes of highly mobile annexin-V molecules during membrane-binding and
98 self-assembly at model membranes and derive its kinetic and energetic terms.
99 Additionally, HS-AFM-HS at specific positions in the annexin lattice where the
100 freedom of movement is restricted to rotation allowed to determine the interaction
101 free energies of protein-protein contacts. The applicability of our technique is wide
102 and is discussed in the end of the manuscript.

103

Results:

Reduced dimensionality leads to ms and µs HS-AFM

106 Annexin-V has been shown, among other functions,[21] to play an important role in
107 membrane repair of eukaryotic cells.[22] The influx of Ca^{2+} from the outside of the cell
108 that occurs upon membrane lesion leads to the rapid tripartide Annexin-V-Ca^{2+}-
109 membrane-binding and self-assembly of Annexin-V into 2D-crystals, surrounding the
110 membrane-defect to prevent further pore expansion.[22] Interactions between
111 annexins, negatively charged phospholipids and Ca^{2+} have been the subject of
112 many studies.[23,24,25] In solution Annexin-V alone has been shown to have a low
113 Ca^{2+}-affinity (~330µM), whereas in the presence of a negatively charged
114 phospholipids the Ca^{2+} affinity increases greatly with two distinct affinities (~2.4µM
115 and 170µM).[26,27] Whilst binding and final assemblies have been well
116 characterized[27,28] no techniques are able to capture the full process and bridge
117 between binding to the membrane, oligomerization and 2D self-assembly into a
118 functional lattice structurally and quantitatively.

119 HS-AFM imaging of supported lipid bilayers (SLBs) containing 20%
120 phosphatidylserine (**Fig. 1a**) shows how annexin binding to surface of membrane

121 (upper leaflet) and subsequent self-assembly occurs over the second timescale
122 (**Fig. 1b**). Assembly of Annexin-V from solution was initiated by illuminating the
123 sample with UV to release Ca^{2+} from a photo-cleavable $EGTA-Ca^{2+}$-complex
124 (**Fig. 1b,c**). Annexin was observed binding to the membrane within a few seconds,
125 reaching full membrane coverage after 32s and 2D-crystal (p6-symmetry)[27] formation
126 within 40s. However, 2D-scanning is not able to resolve the highly mobile membrane-
127 bound annexin trimers (A5) during the early stages of the assembly process, as they
128 diffuse too quickly to be resolved when images are acquired at frame rates of $1s^{-1}$ to
129 $10s^{-1}$; instead, only streaks in the fast scanning direction (x) are observed (herein A5
130 is used to refer to the membrane-bound trimeric form of annexin-V). The average
131 height and abundance of these streaks across the membrane patch can be used to
132 approximate the surface coverage over time (**Fig. 1c**); however such measurements
133 are prone to error due to tip parachuting (where the tip loses contact with the sample
134 and takes some time to return to the surface) and tip induced movement of the
135 proteins. The maximum HS-AFM imaging rate for a typical 100x100 pixel 2D-scan is
136 50-100ms. Each image is scanned left to right and right to left, thus at 50ms per
137 image, 400,000 pixels at which deflection and height are detected are acquired per
138 second (one every 2.5μs).

139   To obtain 100 times improved temporal resolution the slow-scan axis (y-
140 direction) is halted (**Fig. 1d**) and fast-scan axis lines (x-direction) are acquired every
141 0.5-1ms. This produces single line height data (x, z, t), termed line scanning (HS-
142 AFM-LS), in which all of the traces in the x-direction are over the same y-position.
143 One A5, at the p6-axis of the annexin-V 2D-crystal, is free to rotate and has two
144 preferred orientations (**Fig. 1e**, inset).[27] Performing HS-AFM-LS across the annexin
145 lattice (**Fig. 1d**, bottom) we can visualize A5 rotation (**Fig. 1e**). The rotation is most
146 evident for those trimers where the scan line crosses precisely one protomer of the
147 trimer (**Fig. 1d,e**; highlighted with *)). Capturing lines at 2.4ms per line over several
148 seconds shows negligible drift in x-y, as observed by the two stable lines (**Fig. 1e**, at
149 x=4nm and x=16nm) originating from the stable neighboring annexins in the p6-
150 lattice. By contrast, the central region shows rapid flickering between two states
151 above and below x=10nm (**Fig. 1e**). Comparison to a model line-scan across a
152 rotating trimer shows identical switching behavior caused by clockwise and counter-
153 clockwise rotations (**Supplementary Fig. 1**). Analysis of the periods of time spent in
154 each state before rotation (**Fig. 1f**) shows a wide distribution best fit by three
155 Gaussians (as determined by reduced chi-squared values) peaking at 13ms, 41ms
156 and 96ms suggesting possibly three different modes of interaction with the
157 surrounding lattice, that we tentatively assign to the three possible interaction sites of
158 the rotating trimer with its environment.

159   Whilst HS-AFM-LS provides single-digit millisecond temporal resolution, it is
160 still not fast enough to capture microsecond events. Therefore, to gain a further 100-
161 fold time-resolution we also halt the x-piezo to capture Angstrom accuracy height
162 data (z, t) with ~10μs temporal resolution (**Fig. 1i, Supplementary Fig. 2**). This
163 method, termed high-speed AFM height spectroscopy (HS-AFM-HS, **Fig. 1h**), has
164 the temporal resolution to measure the mobility of membrane bound molecules as
165 they diffuse under the tip. A typical height vs. time trace obtained at the surface of an
166 SLB with A5 diffusing on the surface (**Fig. 1i**) gives a signal time series of many
167 sharp peaks of up to ~2nm height, corresponding well to the height of membrane-
168 bound A5. A distribution of heights between H_T and ~2nm is observed due the z-
169 feedback not being able to fully respond to the shorter dwell-times
170 (**Supplementary Fig. 2c**). For future applications of even faster events, the

4

171 amplitude damping of the cantilever oscillation can be monitored, which should report
172 about events beyond the feedback bandwidth. This data was captured at the tapping
173 frequency of the cantilever 625kHz (1.6µs), with feedback settings set to maximize
174 the z-piezo response time (**Supplementary Fig. 2**). Measuring the time duration of
175 each peak above H_T gives a distribution of dwell-times corresponding to the range of
176 times molecules spend under the tip (**Fig. 1j**), with the fastest events being only
177 ~10µs long.
178
A5 diffusion and oligomerization measured by HS-AFM-HS
180   For proteins undergoing 2D Brownian diffusion, the dwell-time τ_D, of the
181 molecule in a detection area is dependent on the protein's diffusion coefficient (D),
182 and the width of the detection area w, by eq. 1.[29]

183 $$\tau_D = w^2/4D \qquad \text{(eq. 1)}$$

184   For techniques such as FCS, the detection area is defined by a fluorescence
185 spot size much larger than the molecules of interest, leading to the protein
186 dimensions having a negligible contribution to τ_D. For HS-AFM-HS however, the
187 inverse is true; the detection area, which is essentially the AFM tip radius (~1nm; we
188 know this because substructures on the proteins can be resolved, see **Fig. 1d**), is
189 typically much smaller than the size of the single diffusing proteins (~10nm diameter)
190 and thus dwell-times are mainly dependent on the molecule size. For molecules
191 undergoing self-assembly the increase in the 2D-area is thus linear with each
192 additional molecule n associated to the aggregate, and therefore τ_D increases
193 proportionally with n. Performing height spectroscopy on A5 molecules undergoing
194 self-assembly into higher order oligomers is therefore expected to produce the multi-
195 peaked distribution of dwell-times we observe in **Fig. 1j**, which not only depends on
196 oligomer size but also its size-dependent diffusion rate (see Supplementary Table 1
197 for full details of oligomer dimensions). The τ_D distribution is well approximated by
198 Gaussian fits however the exact underlaying distribution is expected to be Lévy in
199 nature with heavy tailed probability distributions. The diffusion coefficient D can then
200 be determined from the expected protein dimensions, tip radius and τ_D
201 (Supplementary Table 1).
202   In addition to the oligomer size and diffusion characteristics we can also
203 measure the surface concentration of protein, based on the probability that a
204 molecule is present under the tip at any given time. This probability can be
205 determined by the fraction of time the height z, is above a threshold value H_T
206 ($t_{z>HT}/t_{total}$), and converted into a surface density c (molecules μm^{-2}) based on the
207 molecule size, d_p, via the following relation:

208 $$c = \frac{t_{z>H_T}}{t_{\text{total}}} \cdot \frac{1}{d_p^2} \qquad \text{(eq. 2)}$$

209   The threshold height H_T was not an arbitrary value but chosen based on the
210 background noise level of the height trace, significantly far away from the noise
211 distribution at 5σ so that the probability of mistaking diffusion events is 0.00006%
212 (typically this corresponds to $H_T = 0.8 \pm 0.1$nm (s.d.)).
213   To assess the kinetics of the 2D-assembly process of A5 at membranes, we
214 varied the bulk concentration of calcium with a fixed annexin-V solution
215 concentration. HS-AFM-HS on hydrated SLBs in the absence of Ca^{2+} (**Fig. 2a**) gives
216 a random height noise trace that fluctuates with typical RMS amplitude of 0.17nm,
217 sampled at cantilever resonance frequency of 625kHz. The introduction of 50µM

218   CaCl$_2$ to the bulk phase (**Fig. 2b**) resulted in a small number of infrequent (~6s^{-1})
219   sharp peaks above noise corresponding to single molecule diffusion events under the
220   tip. Assessment of the time fraction gave an A5 surface concentration of 1.0
221   molecules μm^{-2} ± 0.6 (s.d.) whilst analysis of individual dwell-times gave a distribution
222   with a dominant Gaussian peak at ~33 ± 26μs (s.d.), with small and less significant
223   peaks at ~80μs and ~125μs. This τ_D distribution implies a dominant species diffusing
224   on the membrane with a diffusion coefficient D of 0.8 ± 0.6μm^2 s^{-1}, assuming the
225   trimeric form (A5) of membrane-bound annexin. This assumption can be made based
226   on previous studies which suggest that annexin molecules exist in monomeric form
227   only in solution, forming stable trimers almost instantaneously in the presence of Ca^{2+}
228   and anionic lipids as they bind to the membrane.[30] Additionally, the expected dwell-
229   time under the tip for a single protomer diffusing at 1μm^2 s^{-1} would be 2.7μs, outside
230   the z-feedback response time and therefore would not be detected. Inversely, a
231   dwell-time of 33μs for a single annexin-V protomer would imply an unrealistically slow
232   diffusion coefficient of 0.08μm^2 s^{-1} (for the full molecular diffusion/size range currently
233   accessible by HS-AFM-HS see **Supplementary Fig. 3**). A5 diffusion has previously
234   been shown to be of the order 1μm^2 s^{-1} using FRAP,[31] in good agreement with the
235   0.8 ± 0.6μm^2 s^{-1} found here.

236   As the Ca^{2+}-concentration was increased from 50μM to 100μM, 150μM and
237   200μM (**Fig. 2c,d,e**) we observed increases in both the frequency and dwell-times of
238   events; equating to a three orders of magnitude increase in the surface density of A5
239   from 1.0 ± 0.6 to 285 ± 150 A5 μm^{-2}. The increase in surface density can also be
240   seen qualitatively by the occurrence of streaks in HS-AFM images because the
241   molecules diffuse too fast for the HS-AFM to capture whilst 2D-scanning. Analysis of
242   the height spectroscopy events shows the emergence of additional Gaussian peaks
243   at 80 ± 25μs and 130 ± 34μs. Taking the additional peaks to be dimers (A5$_2$) and
244   trimers (A5$_3$) of A5, we can determine A5$_2$ and A5$_3$ diffusion coefficient of
245   0.63 ± 0.21μm^2 s^{-1} and 0.58 ± 0.16μm^2 s^{-1}, respectively, which - as expected for larger
246   molecules - is less than the A5 diffusion coefficient of 0.8μm^2 s^{-1}. We observe small
247   shifts of all peaks to longer dwell-times as a function of the Ca^{2+}-concentration, eg the
248   primary A5 peak shifts from ~33μs to ~37μs and the secondary A5$_2$ peak from ~78μs
249   to ~85μs, which we interpret as the result of crowding when the 2D density of A5
250   increases on the membrane leading to a slow-down of the diffusion rates.

251   Increasing the Ca^{2+}-concentration to 250μM (**Fig. 2f**) resulted in the onset of
252   2D-crystallization. This can be observed both in imaging mode, as a p6-lattice 2D-
253   crystal partially covering the membrane, and in height spectroscopy mode, by the
254   much longer-lived events, which last several tens of milliseconds, as the crystal
255   assembly and disassembly is detected under the tip. Under these conditions, in
256   addition to the three peaks at ~33μs, ~80μs and ~130μs detected at lower Ca^{2+}-
257   concentrations (**Fig. 3b-e**), significantly larger peaks at longer dwell-times at
258   200 ± 60μs and 315 ± 100μs are detected (**Fig. 3f,** right). Because the dwell-time
259   distributions are short and almost mono-disperse at very low surface concentrations
260   (**Fig. 2b,c**, right), and are more and more convoluted with increasing bulk Ca^{2+}-
261   concentration and increasing A5 surface concentration (**Fig. 2d-f**, right), we assign
262   the underlying peaks to A5, dimers of trimers A5$_2$, trimer of trimers A5$_3$, and so on,
263   A5$_4$, A5$_5$, and higher order oligomers (A5$_O$), and thus use these molecular
264   dimensions to determine the oligomer size-dependent diffusion coefficients
265   (**Supplementary Fig. 4**). Diffusion constants, derived from the dwell-time peaks,

266 show a decrease with increasing oligomer size, consistent with the Saffman-Delbrück
267 approximation.[32]

$$D \sim \ln({}^{1}/_{r_{\mathrm{p}}}) \qquad \text{(eq. 3)}$$

269 Since the height/time traces have only Angstrom-range noise (**Fig. 3a**), the
270 occurrence of molecular diffusion events with varying dwell-times (**Fig. 3b,c,d**) are
271 unambiguously detected and allow to determine what oligomeric species are present
272 and at what abundance dependent on the environmental conditions or the overall 2D-
273 concentration on the membrane. The changes in overall surface concentration and
274 oligomer distribution with varying Ca^{2+}-concentration (**Fig. 3e**) indicate that in the
275 presence of up to 100µM Ca^{2+}, annexin-V molecules are predominantly in the trimeric
276 A5 form. At higher Ca^{2+} (150-200µM) significant fractions of A5 encounter other A5
277 and convert into dimers of trimers $A5_2$. At calcium concentrations that permit 2D-
278 crystallization (250µM), we observe reductions in the fractions of both the A5 and $A5_2$
279 populations with significant increases in the fraction of trimers of trimers $A5_3$ and
280 larger oligomeric structures $A5_o$.

281 The total fraction of time molecules spend under the tip during a given period
282 allows the determination of surface concentration. Here, the average surface
283 concentration of A5 grew exponentially with bulk Ca^{2+}-concentration (**Fig. 3e**). The
284 determined surface concentration combined with knowledge of the bulk concentration
285 allows calculation of a partition coefficient, $P = [c_{solution}]/[c_{surface}]$, and hence the
286 free energy associated with annexin-V binding to the membrane, following $\Delta G_0 = $
287 $k_B T \cdot \ln(P)$. These calculations give free energies that decrease with increasing
288 calcium concentration (indicating stronger binding), with values of -1.7k_BT, -3.1k_BT
289 and -6.1k_BT at 50µM, 100µM and 150µM $CaCl_2$ respectively, reaching a minimum of -
290 10.9k_BT at 250µM $CaCl_2$ in agreement with previous studies.[26]

291 Next, we investigated the binding of A5 depending on variations of the bulk
292 annexin-V concentration in presence of saturating 2mM Ca^{2+}-conditions
293 (**Supplementary Fig. 5**). Analogous to the A5 surface binding behavior at varying
294 Ca^{2+}-concentrations, the average surface concentration increased exponentially with
295 bulk annexin-V concentration, and higher oligomeric states accumulate (**Fig. 3f**).
296 Binding free energies, as determined by partition coefficients in saturating Ca^{2+},
297 decrease with increasing bulk annexin-V concentrations from -4k_BT and -6k_BT at 23-
298 35nM and 58-81nM annexin-V respectively, reducing to -7.7k_BT at 103nM before
299 reaching a minimum of -10.9k_BT at 127nM annexin-V. When the data from all bulk
300 annexin-V concentrations is combined (**Fig. 3g**) we observe how the average dwell-
301 times change from dilute surface concentrations, in which the average dwell-time
302 increases gradually with surface concentration, to higher surface concentrations,
303 where the dwell-times increase more rapidly with surface concentration. This
304 transition occurs at approximately 500 A5-molecules µm^{-2} (~3% surface coverage)
305 (**Fig. 3g**, dashed line and kink in the data point distribution). We interpret this in the
306 following way: At low surface concentrations, molecules diffuse freely predominantly
307 in their A5 state. The minor dwell time increase may be related to a slight slow down
308 of diffusion due to the onset of crowding. However when a critical surface
309 concentration is reached (~3%) the encounter probability increases significantly and
310 protein-protein interactions become significant, and higher oligomers are formed. For
311 experiments in varying Ca^{2+} concentrations, fitting to the A5 surface concentration vs.
312 Ca^{2+} bulk concentration (**Fig. 3e**) show this critical A5 surface coverage is reached at
313 240 ± 10µM Ca^{2+}, in agreement with previous work on model membranes and

7

cells.[26,33] Assignment of the dwell-time distribution peaks (**Fig. 2**, right column) to oligomer sizes allows the populations of each oligomer species to be investigated and plotted as a function of surface concentration (**Fig. 3h**). As the A5 surface concentration increases, the fraction of A5 molecules in a single trimer form decreases, whilst the fractions of assemblies composed of 2 ($A5_2$), 3 ($A5_3$), 4 ($A5_4$) and higher oligomeric states ($A5_o$) each increase at successively higher surface coverages. Near the critical surface concentration (500 molecules $\mu m^{-2;}$ ~3% surface coverage), the populations of the $A5_2$, $A5_3$ and $A5_4$ reach maximal fractions at successive surface concentrations before decreasing and giving rise to higher order oligomers, which become the dominant population as the 2D-lattice begins to form.

Oligomerization of A5 at the membrane is a 2D reaction in which the concentration of each oligomer species, [AB] is a function of the surface density of its component parts, [A] and [B]. Thus, under equilibrium conditions, the kinetics can be described by 2D-dissociation constants, K_d.

$$[AB] = [A][B]/K_d \qquad \text{(eq. 4)}$$

For instance, the dimer dissociation constant, $K_{d2} = [A5] \cdot [A5]/[A5_2]$, is defined in terms of the equilibrium surface densities of A5, and $A5_2$. Whilst the trimer dissociation constant, $K_{d3} = [A5] \cdot [A5_2]/[A5_3]$, is dependent on the A5, $A5_2$, and $A5_3$ concentrations. Fitting oligomer concentration data (**Supplementary Fig. 6**) to eq. 5 allows experimental determination of K_d.

$$fraction \ of \ [B] \ in \ complex = \frac{[AB]}{[AB]+[B]} = \frac{[A]}{[A]+K_d} \qquad \text{(eq. 5)}$$

The K_d values obtained from these fits are organized into an AxB matrix for the resulting oligomers of size [AB] (**Table 1**). The dissociation constants K_{dn} obtained for the formation of $A5_2$, $A5_3$, and $A5_4$ are comparable and average to $250 \pm 70 \mu m^{-2}$ (+ 95% CI) suggesting similar interaction strengths between different oligomers.

Computation of the surface concentration dependent populations of each oligomer species using the experimentally determined K_d values (**Supplementary Fig. 6**) shows how the fractions of higher order oligomers change in a stepwise manner (**Fig. 3i**). As the overall surface concentration increases, the fraction of monomers decreases, followed by peaks in population for n=2 (at concentrations close to $K_{d2} = 220 \mu m^{-2}$), n=3 and n=4 as the population of each new higher order structure (n+1) is able to assemble depending on the abundance of the previous one. These characteristics are in close agreement with the experimental populations (**Fig. 3h**).

From ratios between different oligomer species it is possible to estimate a free energy difference between oligomer states, $\ln(c_n / c_m) = \Delta G/k_B T$ (**Supplementary Fig. 7**), where c_n and c_m are the surface concentrations of oligomers constituted of n and m A5s, respectively.

Rapid A5 membrane binding precedes oligomer assembly

By using the photosensitive caging compound NP-EGTA to cage calcium we can simulate the burst of Ca^{2+} that would occur in a cell when the plasma membrane was injured, to follow the annexin binding and oligomerization over time[27] to an initially bare membrane (**Fig. 4a**). Upon UV-illumination, we observed under the here used experimental conditions (1mM caged-Ca^{2+} and 200nM annexin-V in solution) single A5 diffusion events after 2.8s (**Fig. 4b,d,e,f**). In the beginning, the frequency number of events increased linearly with time (**Fig. 4g,** red line) before more

8

361 dramatically increasing and fluctuating as a function of time, reaching a maximum of
362 2600s⁻¹ after 73s illumination, when 2D-crystallization sets in. Additionally, the
363 average residence time under the tip of each event, initially relatively constant around
364 40μs, in agreement with single A5 diffusion (see figures 2 and 3b), increased and
365 fluctuated similarly to the event count rate as the membrane gets crowded, in
366 agreement with the formation of higher order oligomers. Surface concentration
367 measurements show a gradual increase over time (**Fig. 4h**, red line) before sharply
368 increasing as a critical concentration of 400-600 molecules μm^{-2} is reached, in
369 agreement with the pooled data equilibrium experiments (see figure 3g). Analysis of
370 the oligomer distribution over time indicates that this sharp increase coincides with a
371 sudden onset in the fraction of oligomers composed of 5 or more A5. After 100s UV-
372 illumination, HS-AFM imaging showed the resulting complete p6-lattice of A5 with no
373 apparent perturbation caused by the HS-AFM-HS measurement (**Fig. 4c**).

374

Single A5 rotational dynamics revealed by HS-AFM-HS & -LS

376 Once the A5 p6-lattice is assembled, it contains two-thirds p6-trimers that
377 constitute the honeycomb lattice and one-third non-p6 trimers that are not strictly part
378 of the lattice being trimers sitting on the 6-fold symmetry axis (**Fig. 5a**, see also
379 figures 1d). The non-p6 trimers only weakly interact with the p6-lattice at two
380 preferred orientations at 0° and 60° (**Fig. 5b**).[27] The interaction is weak enough such
381 that it allows rotational freedom intermittently resolvable by HS-AFM imaging
382 (**Fig. 5a**, **Supplementary Movie 1**). Measuring this rotational freedom provides a
383 means to determine non-p6-trimer interactions with neighboring molecules and
384 directly compare dynamics observed by line scanning with HS-AFM-HS. Positioning
385 the tip on one of the protomers of a non-p6 trimer and performing HS-AFM-HS gives
386 a height trace that fluctuates over time between two distinguishable states with
387 heights of 2.00±0.10nm (mean ± s.d.) and 1.72±0.07nm (**Fig. 5c**). Performing HS-
388 AFM-HS on immobile trimers in the hexagonal p6-lattice produced a height trace with
389 only one state (± 0.12nm). It should be noted the scanner stage can drift by some
390 nanometers in x- and y-dimension, especially during the seconds after execution of a
391 position or scan range change due to piezo-relaxation. To assess the mechanical
392 drift, we can capture HS-AFM images of the A5-lattice for several minutes and then
393 use image correlation alignment software to find the x-y translations required to align
394 the image set. Under normal imaging conditions the total drift distance was found to
395 vary from as low as 0.02nm s⁻¹ with a well-equilibrated system (as shown in
396 **Supplementary Fig. 8, Supplementary Movie 2**) up to 0.1nm s⁻¹. This drift is
397 relatively slow (10-50s nm⁻¹) in comparison to the tip radius, the area of interest and
398 the biological dynamics to be analyzed (>>10s⁻¹) and suggests that HS-AFM-HS can
399 be positionally accurate for 10s of seconds. Such stability provides an additional
400 advantage of HS-AFM-HS and HS-AFM-LS over fluorescence techniques where
401 bleaching often limits the total time a molecule can be observed with high temporal
402 resolution.

403 Performing line scanning across the non-p6 trimer (as depicted by the dashed
404 line in **Fig. 5a,b**) produces kymograph images displaying time (x-axis), position (y-
405 axis) and height (color scale) (**Fig. 5d**, top). The line scan kymograph detects the
406 non-p6 trimer primarily at one of two positions ~3nm apart in y as shown by the labels
407 marked 0° and 60°. Over time flickering between the two states is observed. Plots
408 show how the heights in these positions fluctuate around ~1.8nm and ~2.0nm over
409 time for both the 0° and 60° positions (**Fig. 5d**, green and red traces). These height

410 changes closely comparable to those obtained by HS-AFM-HS (**Fig. 5c**). However,
411 because the line scanning measurement captures data at two different regions of
412 interest that behave in an anti-correlated manner with each other, taking the
413 difference between the two height traces can be used to amplify the signal whilst
414 reducing any correlated error that occur in both traces. This produces an enhanced
415 signal-to-noise ratio (**Fig. 5d**, black trace) with two distinct states (**Fig. 5g**). The
416 movements between the 0° and 60° states, detected by HS-AFM-HS and line
417 scanning result in average dwell-times of 26 ± 3ms (s.e.m., n = 401) and 35.0 ± 1ms
418 (s.e.m., n = 2053), respectively (**Fig. 5f**). This difference, measured by the two
419 methods, is likely due to the greater energy input via the tip in HS-AFM-HS combined
420 with the higher temporal resolution of HS-AFM-HS which was able to detect dwell-
421 times as short as 240µs, beyond the time resolution of line scanning.

422   Although HS-AFM-HS offers higher temporal resolution, the ability of line
423 scanning to also measure position allows direct visualization of the rotational velocity
424 of the trimer (**Fig. 5e**). Line scanning kymographs reveal linear transitions in time
425 from the 0° to the 60° or vice versa. As visible in raw data (**Fig. 5e**, top) and
426 corroborated by model line scanning rotations (not fitted to the data) (**Fig. 5e**,
427 bottom), the characteristics of these transitions depend on the initial state and the
428 direction of rotation (**Supplementary Fig. 1**). Rotations were observed to occur in
429 both clockwise and counter-clockwise directions with an average time of 18 ± 6ms,
430 corresponding to a rotational velocity of 3300°s^{-1} (550rpm) (**Fig. 5e**, right). As
431 expected by the symmetry of the system, the non-p6 trimer showed no preference for
432 either the 0° or 60° state and as such, there is no free energy diffe rence between
433 states. We can however estimate a free energy barrier that is overcome between the
434 0° and 60° states o f ~$0.7k_{B}T$ ($\pm$ $0.4k_{B}T$ (s.d.)), using the average time spent in each
435 state and the average time the trimer is rotating, following.

436
$$\Delta G = -\ln\left(\tau_{rotation}/\tau_{state}\right)k_{B}T \qquad \text{(eq. 6)}$$

437 **Conclusions**

438 In this work, we have developed and applied two HS-AFM techniques, HS-AFM line
439 scanning and HS-AFM height spectroscopy (HS-AFM-HS), which allow Angstrom-
440 precision dynamic measurements of single molecules at millisecond- and ~10µs-
441 timescales, respectively. These advances allow us to capture biologically relevant
442 rapid diffusion of unlabeled molecules over a full range of concentrations and at
443 length- and time-scales not accessible to other techniques.

444   HS-AFM line scanning detects nanoscale movements at millisecond rates,
445 here the A5 rotation, reported by ~0.3nm height variations between the tip of the
446 protomers and the connections in between. HS-AFM height spectroscopy (HS-AFM-
447 HS), an approach inspired by fluorescence spectroscopy, measures height changes
448 at microsecond rates as molecules move under the tip, here the diffusion of
449 molecules and gives information about diffusion rates, surface concentrations, and
450 oligomerization of unlabeled biomolecules. A small number of previous studies have
451 also shown the potential of reducing the dimensionality of acquisition in AFM as a
452 tool to study dynamics, however it is yet to be fully exploited.[34-39]

453   Together; the data allows us to describe the entire annexin-V membrane
454 association and self-assembly process in quantitative detail (**Fig. 6**). Initially at low
455 Ca^{2+} concentrations, single A5 diffuse on the membrane with 0.8µm^{2} s^{-1}, upon further
456 recruitment of A5, higher oligomers form on the membrane notably A5$_2$ and A5$_3$ that
457 diffuse slower with 0.63µm^{2} s^{-1} and 0.58µm^{2} s^{-1}, respectively. These multimeric states
458 exist in equilibrium with each other implying interactions are reversible and weak

459 (comparable to thermal energy). As the surface concentration increases further,
460 crowding lowers slightly the diffusion of A5 (~10%) and A5$_2$ (~8%) and allows the
461 formation of even higher oligomers A5$_4$ and A5$_5$ that diffuse slower than the smaller
462 oligomers with 0.50µm^2 s^{-1} and 0.46µm^2 s^{-1} respectively. These higher-order
463 oligomers are formed in a stepwise manner consistent with self-assembly models of
464 2D-association. As higher order oligomers accumulate, and higher surface densities
465 are attained, a critical 2D-concentration of ~500 molecules µm^{-2} is reached leading to
466 the formation of an immobile lattice. At this critical concentration when higher-order
467 structures form, surface binding from the bulk increases significantly. This may be
468 either a consequence of the lattice formation, which allows capture of the molecules
469 into a structure where k$_{off}$ (in both 2D and 3D) becomes extremely low, or that the
470 increased binding triggers lattice formation. It seems very likely that the integration of
471 A5 into larger-scale supramolecular structures significantly lowers the k$_{off}$ due to a
472 form of avidity where molecules in the lattice stabilize other molecules in the lattice.
473 In support of this, we found using HS-AFM imaging during Ca^{2+} titration (addition and
474 removal) that the lattice trimers had a different apparent Ca^{2+} and membrane affinity
475 than the non-p6-trimers.[27] In cellular environments, such a bias may provide a way to
476 spatially regulate lattice formation to the membrane defect.

477   Here, we extend the dynamic range of HS-AFM imaging mode of ~100ms with
478 HS-AFM line scanning (HS-AFM-LS) to ~1ms and with HS-AFM height spectroscopy
479 (HS-AFM-HS) to ~10µs. The z-sensitivity of all modes is solely limited by the
480 precision of the detection of the cantilever deflection which is currently ~1.5Å at the
481 bandwidth limit of the cantilever resonance frequency.[40] Using this technical toolbox,
482 we measure rapid diffusion processes, giving access to biochemical and biophysical
483 parameters including affinities and association/dissociation kinetics describing
484 entirely and quantitatively the Annexin-V membrane-association process.

485   HS-AFM-LS and HS-AFM-HS have a wide range of applications to study
486 microsecond dynamics of unlabeled biomolecules, such as the study of ligand-
487 induced oligomerization of receptors and transporters, the conformational dynamics
488 of transporters, receptors and channels during transport cycles, ligand binding and
489 gating, respectively, or diverse enzymatic actions.

490

491 **Methods**

492 **HS-AFM**

493 All AFM measurements in this study were taken by amplitude modulation mode
494 HS-AFM (RIBM, Japan), as previously described in Miyagi et al. 2016.[27] In brief,
495 short cantilevers (USC-F1.2-k0.15, NanoWorld, Switzerland) with spring constant
496 of 0.15N m^{-1}, resonance frequency of ~0.6MHz and a quality factor of ~2 in buffer,
497 were used. The HS-AFM was equipped with an illumination system allowing UV
498 light from a mercury lamp to be focused through the same objective as the HS-
499 AFM IR laser to release caged Ca^{2+} during HS-AFM imaging or HS-AFM-HS.

500

501 **HS-AFM-HS**

502 HS-AFM-HS measurements were taken directly after HS-AFM imaging by stopping
503 the x-y piezos, leaving the tip at the center of the previous image with the z-feedback
504 remaining active. Measurements were taken with a free oscillation amplitude of ~3nm
505 and a set-point amplitude at >90% of the free amplitude. Feedback settings were
506 optimized to maximize feedback response speed. Z-piezo data was captured with

507 home written software and a data acquisition board with a maximum acquisition rate
508 of 2,000,000 samples s^{-1} (LabView programming, NI-USB-6366 card, National
509 Instruments, USA).

510

Sample Preparation

512 The annexin-V used in this study was purchased from Sigma-Aldrich (Annexin-V,
513 33kD from human placenta) and all lipids (dioleoyl-phosphatidyl-choline (DOPC)
514 and dioleoyl-phosphatidyl-serine (DOPS)) from Avanti polar lipids. Annexin binding
515 and crystallization on SLBs was achieved by addition of annexin to a preformed
516 lipid bilayer. In brief, lipids were solubilized in chloroform at a ratio of
517 DOPC:DOPS = 8:2. The solvent solubilized mixed lipids were dried by a nitrogen
518 flow and further dried in a vacuum chamber for 2hr. Then the dried lipid was
519 resuspended into a buffer solution containing 10mM HEPES at pH 7.4, 150mM
520 NaCl and 2mM CaCl$_2$ to form multilamellar vesicles. As the final step in lipid
521 preparation the suspension was tip-sonicated for 10min to obtain small unilamellar
522 vesicles (SUVs). 1.5µl of the SUV solution with a total lipid concentration of 0.1mg
523 ml^{-1} was deposited onto freshly cleaved mica to form SLBs through vesicle
524 fusion. The excess lipids, after SLB formation, were rinsed first with deionized
525 water followed by buffer. A5 was added to the imaging solution at varying volumes
526 to achieve desired bulk concentrations with an observation buffer 10mM HEPES at
527 pH 7.4, 150mM NaCl with CaCl$_2$ ranging between 0-2mM.

528

Ca^{2+} Uncaging Experiments

530 In the Ca^{2+} uncaging experiments, the observation buffer contained 10mM HEPES
531 at pH 7.4, 150mM NaCl, 1mM CaCl$_2$ and 1.25mM o-nitrophenyl EGTA tetra-
532 potassium salt (NP-EGTA). The ensemble of 1mM CaCl$_2$ and 1.25mM NP-EGTA
533 forms 1mM caged Ca^{2+}, the slight excess of NP-EGTA assures complete Ca^{2+}-
534 chelation. NP-EGTA has a high selectivity for Ca^{2+} upon UV illumination, its Ca^{2+}
535 dissociation constant increases 12,500 fold from 80nM to >1mM. During uncaging
536 HS-AFM-HS measurements, UV light from the mercury lamp was allowed to pass
537 through to the AFM-scanning area using a shutter and aperture to control the
538 intensity. The diameter of the UV spot size was around 1mm^2 including the AFM
539 scanning area.

540

Data Analysis

542 The HS-AFM movies were drift corrected and contrast adjusted by a laboratory-
543 built image analysis software in ImageJ. To minimize x-y drift during HS-AFM-LS
544 and HS-AFM-HS, the scanner and tip holder were made sure to be in stable positions
545 and large x-y translations were avoided directly before HS-AFM-HS/HS-AFM-LS data
546 capture. Additionally, to ensure the HS-AFM tip is on the same molecule for a certain
547 period and no significant changes in tip radius has occurred, HS-AFM image sets
548 were captured directly before and after HS-AFM-HS measurements, allowing the
549 total drift to be measured and tip quality to be assessed. The HS-AFM line-scanning
550 kymographs were contrast adjusted and assembled by routines and self-written
551 analysis software in ImageJ. HS-AFM-HS and HS-AFM-LS height/time traces were
552 analyzed using self-written routines in MATLAB (Matlab, Mathworks, Natick, MA,
553 USA).

554

References:

1. Phillips, R., Ursell, T., Wiggins, P. & Sens, P. Emerging roles for lipids in shaping membrane-protein function. Nature **459,** 379–385 (2009).
2. Engelman, D. M. Membranes are more mosaic than fluid. Nature, **438**, 578, (2005).
3. Ronald J. Clarke and Mohammed A. A. Khalid. Pumps, channels and transporters: methods of functional analysis. Anal. Bioanal. Chem. **408,** 7225–7226 (2016).
4. Gouaux, E. & MacKinnon, R. Principles of selective ion transport in channels and pumps. Science, **310**, 1461-1465 (2005).
5. Liao, M., Cao, E., Julius, D. & Cheng, Y. Single particle electron cryo-microscopy of a mammalian ion channel. Curr. Opin. Struct. Biol. **27**, 1–7 (2014).
6. Liang, B. & Tamm, L. K. NMR as a tool to investigate the structure, dynamics and function of membrane proteins. Nat. Struct. Mol. Biol. **23**, 468 (2016).
7. Hell, S. W. & Wichmann, J. Breaking the diffraction resolution limit by stimulated emission: stimulated-emission-depletion fluorescence microscopy. Opt. Lett, **19**, 780-782 (1994).
8. Betzig, E. et al. Imaging intracellular fluorescent proteins at nanometer resolution. Science, **313**, 1642-1645 (2006).
9. Moerner, W. E. & Orrit, M. Illuminating single molecules in condensed matter. Science, **283**, 1670-1676 (1999).
10. Lambert, T. J. & Waters, J. C. Navigating challenges in the application of superresolution microscopy. J. Cell Biol. **216,** 53–63 (2017).
11. Roy, R., Hohng, S. & Ha, T. A practical guide to single-molecule FRET. Nat. Methods, **5,** 507–516 (2008).
12. Holden, S. J., Uphoff, S., Hohlbein, J., Yadin, D., Le Reste, L., Britton, O. J. & Kapanidis, A. N. (2010). Defining the limits of single-molecule FRET resolution in TIRF microscopy. Biophys. J. **99,** 3102-3111 (2010).
13. Kim, S. A., Heinze, K. G. & Schwille, P. Fluorescence correlation spectroscopy in living cells. Nat. methods, **4**, 963 (2007).
14. Mueller, V. et al. FCS in STED Microscopy: Studying the Nanoscale of Lipid Membrane Dynamics. Methods Enzymol. **519**, 1–38 (2013).
15. Kim, J. Y., Kim, C., & Lee, N. K. Real-time submillisecond single-molecule FRET dynamics of freely diffusing molecules with liposome tethering. Nat. Commun. **6**, 6992 (2015).
16. Ruan, Y., Miyagi, A., Wang, X., Chami, M., Boudker, O. & Scheuring, S. Direct visualization of glutamate transporter elevator mechanism by high-speed AFM. Proc. Natl. Acad. Sci. USA, **114**, 1584-1588 (2017).
17. Uchihashi, T. & Scheuring, S. Applications of high-speed atomic force microscopy to real-time visualization of dynamic biomolecular processes. Biochim. Biophys. Acta - Gen. Subj. **1862,** 229–240 (2018).
18. Karner, A. et al. Tuning membrane protein mobility by confinement into nanodomains. Nature Nanotech, **12**, 260 (2017).
19. Miyagi, A., Ramm, B., Schwille, P. & Scheuring, S. High-Speed Atomic Force Microscopy Reveals the Inner Workings of the MinDE Protein Oscillator. Nano Lett. **18,** 288–296 (2018).
20. Ando, T. High-speed atomic force microscopy and its future prospects. Biophys. Rev. **10,** 285–292 (2018).
21. Gerke, V., Creutz, C. E. & Moss, S. E. Annexins: linking Ca 2+ signalling to membrane dynamics. Nat. Rev. Mol. Cell Biol. **6**, 449 (2005).
22. Bouter, A. et al. Annexin-A5 assembled into two-dimensional arrays promotes cell membrane repair. Nat. Commun. **2,** 274–279 (2011).
23. Patel, D. R. et al. The conserved core domains of annexins A1, A2, A5, and B12 can be divided into two groups with different Ca2+-dependent membrane-binding properties. Biochemistry **44,** 2833–44 (2005).
24. Reviakine, I., Bergsma-Schutter, W. & Brisson, A. Growth of Protein 2-D Crystals on Supported Planar Lipid Bilayers Imaged in Situ by AFM. J. Struct. Biol. **121**, 356-362

610   (1998).

611 25. Richter, R. P., Him, J. L. K., Tessier, B., Tessier, C. & Brisson, A. R. On the kinetics of
612   adsorption and two-dimensional self-assembly of annexin A5 on supported lipid
613   bilayers. Biophys. J. **89**, 3372-3385 (2005).

614 26. Gauer, J. W., Knutson, K. J., Jaworski, S. R., Rice, A. M., Rannikko, A. M., Lentz, B. R.
615   & Hinderliter, A. Membrane modulates affinity for calcium ion to create an apparent
616   cooperative binding response by annexin a5. Biophys. J. **104**, 2437-2447 (2013).

617 27. Miyagi, A., Chipot, C., Rangl, M. & Scheuring, S. High-speed atomic force microscopy
618   shows that annexin V stabilizes membranes on the second timescale. Nat. Nanotech.
619   **11,** 783–790 (2016).

620 28. Bouter, A., Carmeille, R., Gounou, C., Bouvet, F., Degrelle, S. A., Evain-Brion, D., &
621   Brisson, A. R. Review: Annexin-A5 and cell membrane repair. Placenta, **36**, S43-S49
622   (2015).

623 29. Fahey, P. F. et al. Lateral diffusion in planar lipid bilayers. Science **195**, 305-306
624   (1977).

625 30. Oling, F., Bergsma-Schutter, W. & Brisson, A. Trimers, dimers of trimers, and trimers of
626   trimers are common building blocks of annexin A5 two-dimensional crystals. J. Struct.
627   Biol. **133,** 55–63 (2001).

628 31. Wagner, M. L. & Tamm, L. K. Tethered Polymer-Supported Planar Lipid Bilayers for
629   Reconstitution of Integral Membrane Proteins: Silane-Polyethyleneglycol-Lipid as a
630   Cushion and Covalent Linker. Biophys. J. **79,** 1400–1414 (2000).

631 32. Saffman, P. G. & Delbruck, M. Brownian motion in biological membranes. proc. Natl.
632   Acad. Sci. USA **72,** 3111–3113 (1975).

633 33. Wang, J. et al. Quantitative analysis of annexin V–membrane interaction by flow
634   cytometry. Eur. Biophys. J. **44**, 325-336 (2015).

635 34. Viani, M. B. et al. Probing protein-protein interactions in real time. Nat. Struct. Mol. Biol.
636   **7,** 644–647 (2000).

637 35. Yokokawa, M. et al. Fast-scanning atomic force microscopy reveals the ATP/ADP-
638   dependent conformational changes of GroEL. Embo Journal **25,** 4567–4576 (2006).

639 36. Yokokawa, M. & Takeyasu, K. Motion of the Ca2+-pump captured. FEBS Journal **278,**
640   3025–3031 (2011).

641 37. Thomson, N. H. et al. Protein tracking and detection of protein motion using atomic
642   force microscopy. Biophys. J. **70,** 2421–2431 (1996).

643 38. Radmacher, M., Fritz, M., Hansma, H. G. & Hansma, P. K. Direct Observation of
644   Enzyme-Activity with the Atomic-Force Microscope. Science **265,** 1577–1579 (1994).

645 39. Pelling, A. E., Sehati, S., Gralla, E. B., Valentine, J. S. & Gimzewski, J. K. Local
646   nanomechanical motion of the cell wall of Saccharomyces cerevisiae. Science **305**,
647   1147-1150 (2004).

648 40. Miyagi, A. & Scheuring, S. A novel phase-shift-based amplitude detector for a high-
649   speed atomic force microscope. Rev. Sci. Instrum. **89**, 083704 (2018).
650

651 **Data Availability**
652 The datasets generated and/or analyzed during the current study are available
653 from the corresponding author on reasonable request.
654

655 **Code Availability**
656 MATLAB codes used for analysis are available from the corresponding author on
657 reasonable request.
658
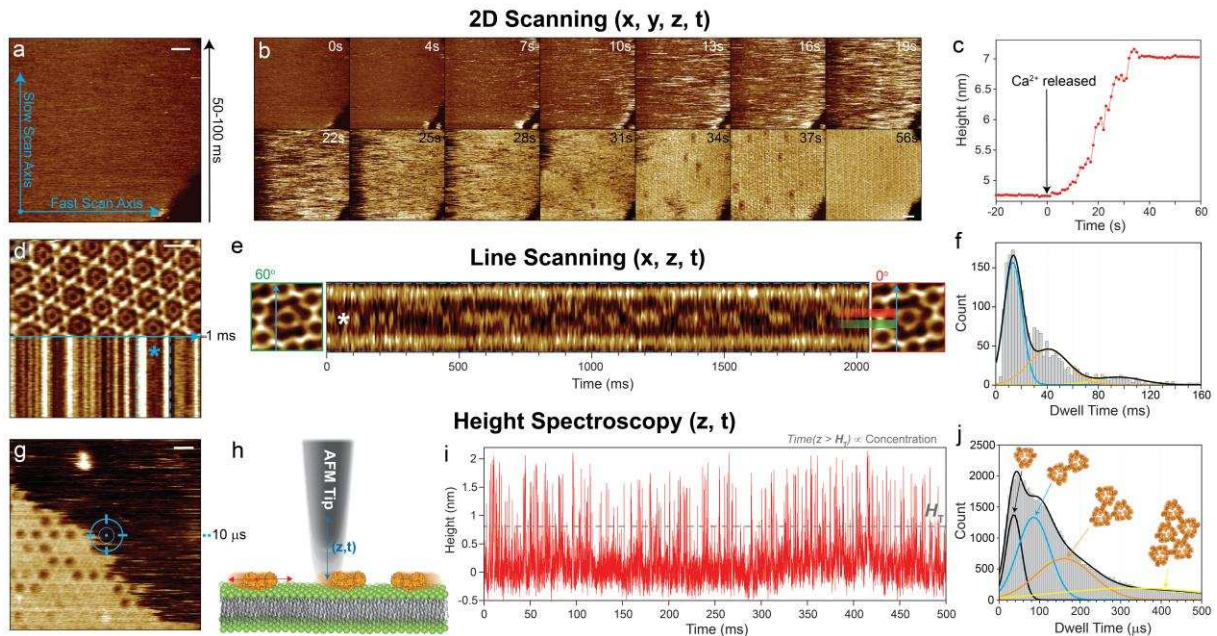
662 **Author Contributions**

14

663 S.S and G.R.H conceived and designed the experiments. G.R.H performed the
664 experiments. S.S and G.R.H analysed the data. S.S and G.R.H wrote the paper.
665

666 **Competing Interests**
667 The authors declare no competing interests.
668

669
670 **Figure 1) Increasing the temporal resolution of HS-AFM by reducing the dimensionality**
671 **of data acquisition. a)** HS-AFM image of a DOPC/DOPS (8:2) membrane in the presence of
672 annexin-V and NP-EGTA-caged Ca^{2+}. Blue arrows illustrate the slow- (vertical) and the fast-
673 scan axis (horizontal). Images can be captured at up to 10-20 frames s^{-1}. **b)** HS-AFM movie
674 frames of A5 membrane-binding, self-assembly and formation of p6 2D-crystals upon UV-
675 illumination induced Ca^{2+}-release. **c)** Average height/time trace of the membrane area in (b).
676 **d)** Averaged HS-AFM image of an A5 p6-lattice overlaid with the subsequent line scanning
677 kymograph, obtained by scanning repeatedly the central x-direction line as illustrated by the
678 blue arrow with a maximum rate of 1000-2000 lines s^{-1}. **e)** Line scanning kymograph across
679 one protomer of the non-p6 trimer, marked by * in (d) and (e) at a rate of 417 lines s^{-1} (2.4ms
680 per line). **f)** Histogram of state dwell-times of the molecule in (e). **g)** HS-AFM image of an A5
681 p6-lattice partially covering a DOPC/DOPS (8:2) SLB surface during self-assembly. HS-AFM
682 height spectroscopy (HS-AFM-HS) is performed following halting the x- and y-piezos to
683 capture height information at a fixed position at the center of the image (illustrated by the
684 target). **h)** Schematic showing the principle of HS-AFM-HS. The AFM tip is oscillated in z at a
685 fixed x,y-position, detecting single molecule dynamics such as diffusion under the tip. **i)**
686 Height/time trace obtained by HS-AFM-HS with the tip positioned at the center of image (g)**.**
687 The height/time trace allows determination of the local A5 concentration analyzing the time
688 fraction of the occurrence of height peaks. **j)** Dwell-time analysis of each height peak of
689 diffusing A5 from 60s height/time data and subsequent fitting of the distribution to multiple
690 Gaussians (possible molecular aggregates corresponding to the fits with distinct dwell-times
691 (τ_D) are shown above the graph). All scale bars: 20 nm.

15
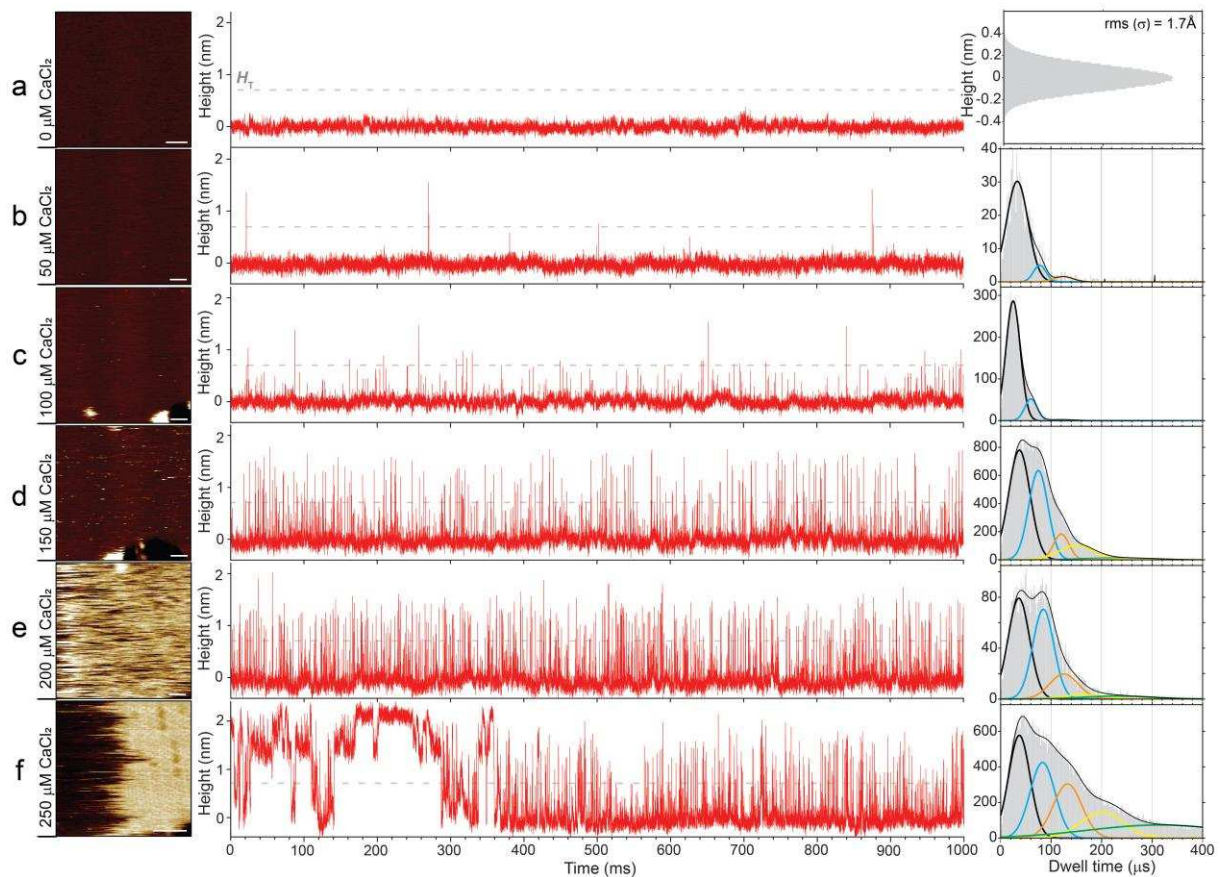
692
Figure 2) HS-AFM-HS of diffusion and self-assembly at model membranes. a) HS-AFM
image frame (left) and height spectroscopy height/time trace (middle) of the membrane (8:2
DOPC/DOPS) surface without Ca^{2+} in solution. The histogram (right) shows the full
distribution of height values detected indicating a noise level of 0.17nm at 625kHz sampling
rate. **b)**, **c)**, **d)**, **e)** and **f)** HS-AFM image frames (left) and subsequent height spectroscopy
height/time traces (middle) at the membrane surface with 50µM b), 100µM c), 150µM d),
200µM e) and 250µM f) Ca^{2+} in solution. Right: corresponding dwell time (τ_D) distributions
with multi-component Gaussian fits. All measurements were performed in the presence of
127nM annexin-V in solution. Images: Full color scale: 4nm, scale bars: 50nm. 1000ms
height/time traces are example sections from longer, typically 60s, traces.

16
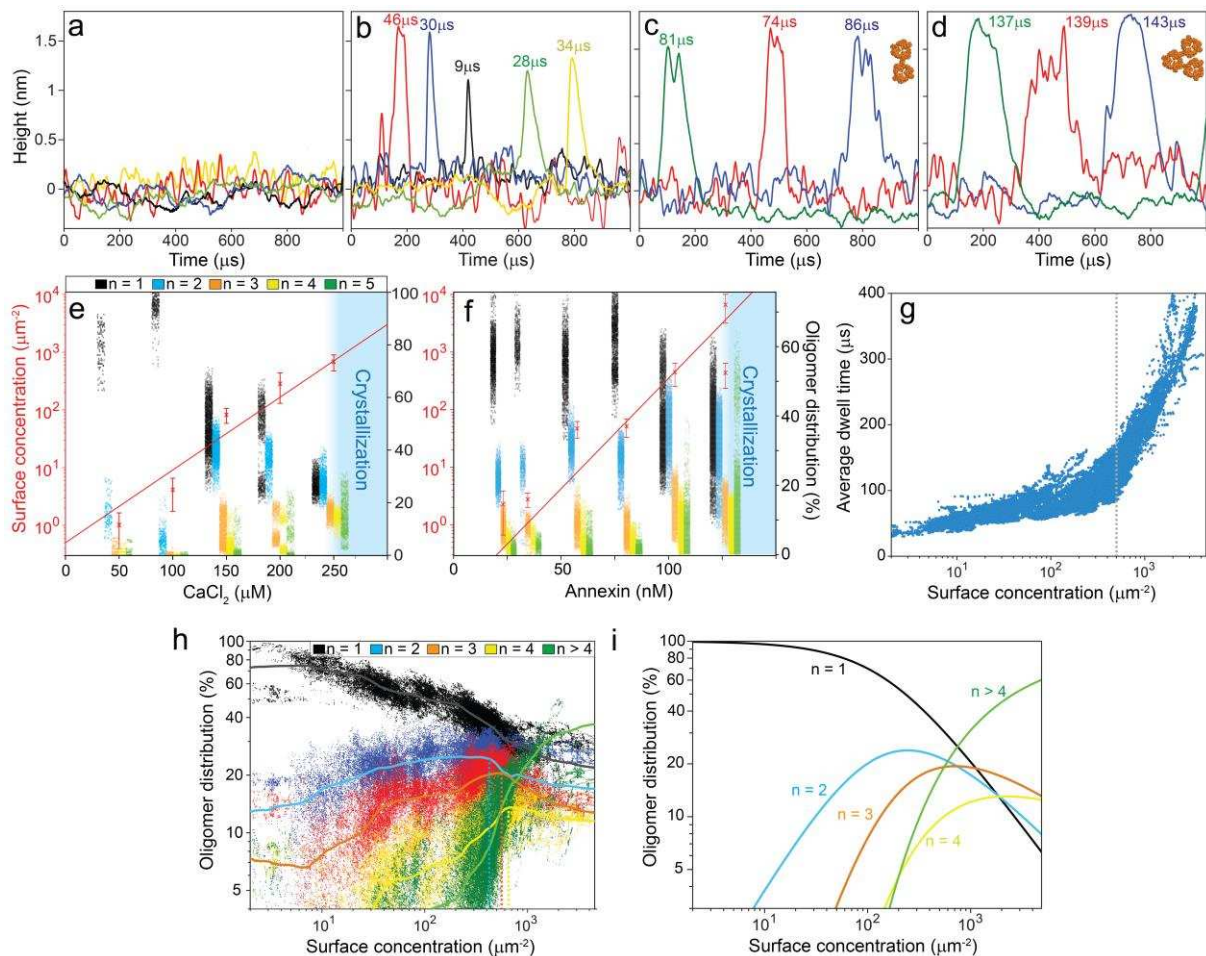
Figure 3) Determination of A5 oligomeric states and dynamics on the membrane. a), **b)**, **c)** and **d)** Overlaid 1ms height/time traces showing background noise (a) and diffusion event peaks around 33µs (b), 80µs (c) and 130µs (d) dwell-times. **(e)** Averaged surface concentrations (mean ± s.d.) and oligomer distributions obtained by dwell-time peak fitting for varying Ca^{2+}-concentrations at constant 127nM annexin-V bulk concentration, and **(f)** at varying annexin-V bulk concentrations at constant 2mM Ca^{2+} concentration. Shaded areas in (e) and (f): concentrations at which self-assembly into 2D-crystals is observed. **g)** Graph displaying the average A5 diffusion dwell-times under the tip as a function of surface concentration. Average dwell-times are calculated from dwell-times observed within 1-second time-windows. At ~500 molecules μm^{-2} surface density (dashed line), the average dwell-times changes regime indicative of the formation of higher order oligomers. **h)** Experimental and **i)** theoretical oligomer distributions as a function of surface concentration. Oligomer distributions in (h) and surface concentrations (x-axes in h and g) are calculated over 1-second time-windows during the height spectroscopy analysis. The oligomer distributions are determined based on the range covered by the dwell-times peaks for each oligomeric state (see Fig. 2, right). Theoretical oligomer distributions were calculated using experimentally fitted equilibrium binding constants (table 1) between A5 and higher order assemblies, $A5_2$, $A5_3$, etc.

17
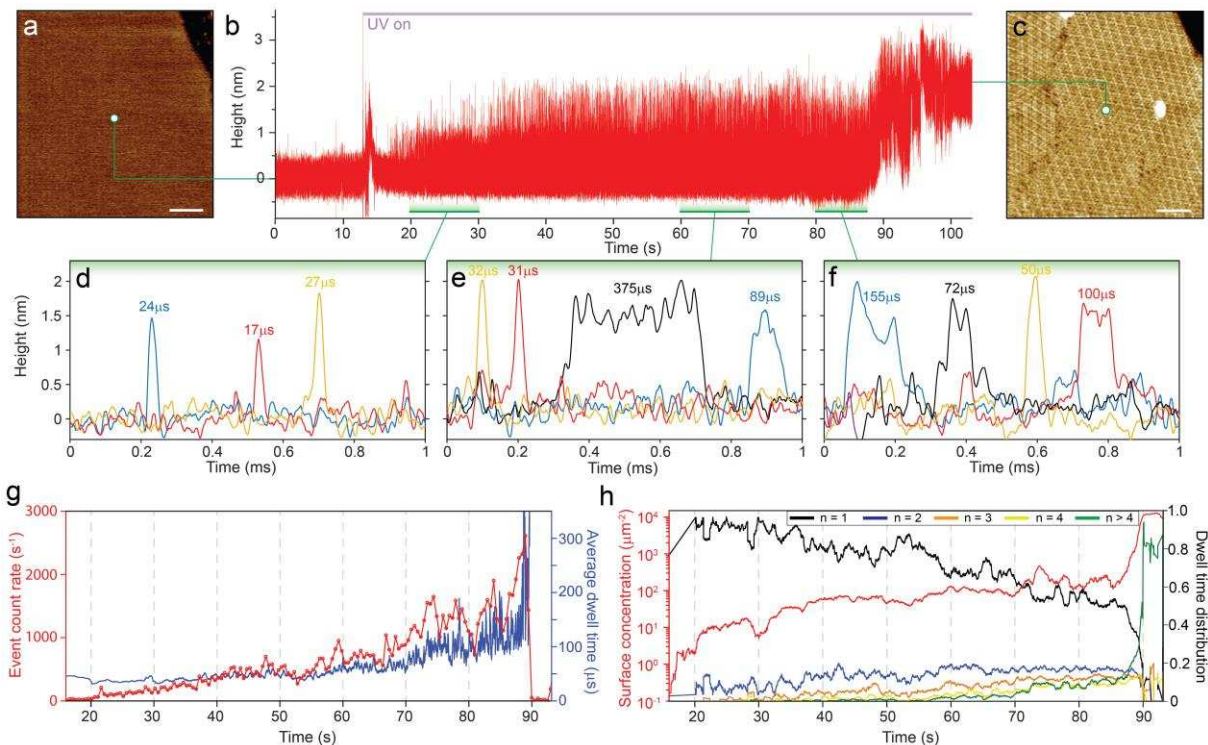
723
Figure 4) Time-lapse HS-AFM-HS of annexin-V membrane-binding and self-assembly.
a) HS-AFM image taken before A5 membrane-binding and self-assembly (bare lipid bilayer).
b) HS-AFM-HS height/time trace during illumination with UV-light to release Ca^{2+}. **c)** HS-AFM
image taken directly after b) (p6-lattice 2D-crystals). **d)**, **e)** and **f)** show higher temporal
resolution zoom-ins of the HS-AFM-HS trace (b) showing example diffusion events from the
20-30s, 60-70s and 80-87s time regions, respectively, with different line colors representing
different events. **h)** Number of single diffusion events (red) and averaged dwell-times (blue)
over time. **g)** Overall surface concentration (red) and oligomer species (black: A5, blue: $A5_2$,
orange: $A5_3$, yellow: $A5_4$, green: $A5_O$) distribution changes over time. Traces in d, and e, are
averaged over 1 second time-windows (time scale panels c, d and e are matched). Scale
bars: 50nm.

735
736

18
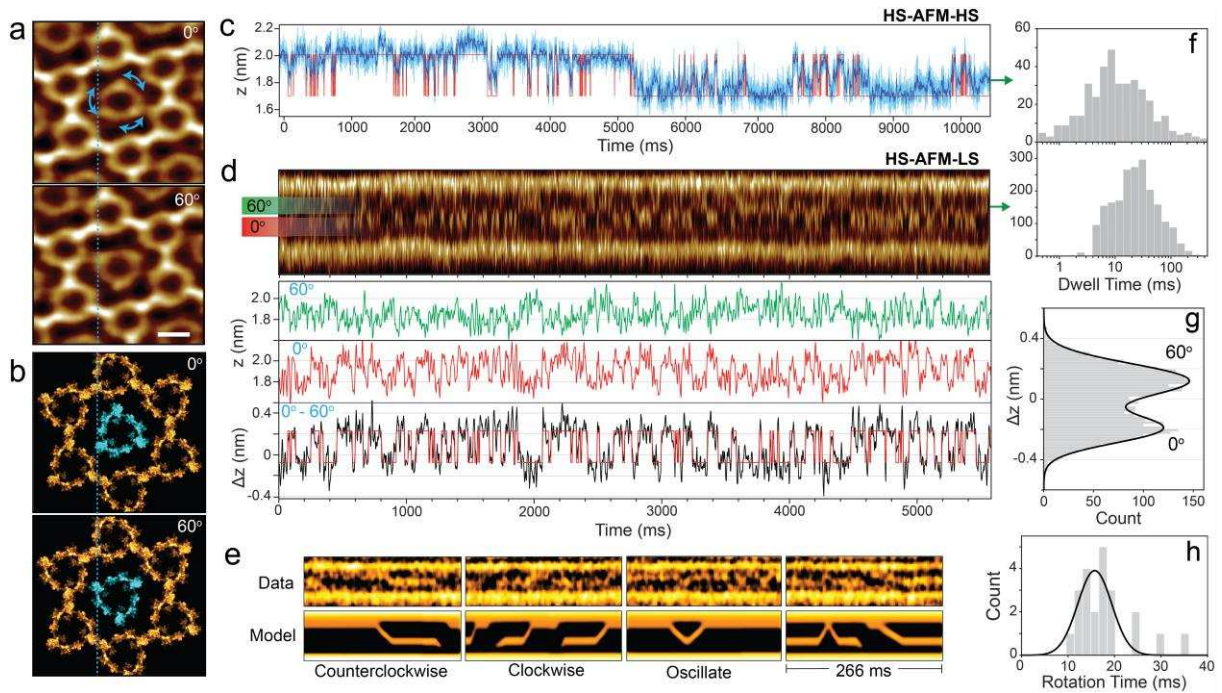
Figure 5) HS-AFM-HS and line scanning of A5 rotation. **a)** averaged HS-AFM images and **b)** structural models, of the A5 trimer at the center of the hexagonal p6-lattice, captured in its two preferred orientations 0º and 60º (Supplementary Movie 1). Scale bar: 5nm. **c)** Height/time trace obtained from HS-AFM-HS measurements on one protomer of the rotating A5. Data was captured at 655kHz (light blue) and was overlaid with filtered data over 30 points (dark blue) and an idealized two state trace (red). **d)** Line scanning kymograph across one A5 protomer captured at 2.4ms per line. Labels 60º and 0 º (see in a) indicate the x-positions where the height/time traces below, in green and red respectively, were obtained. The anti-correlation of the two positions allows the height/time signal difference between the height traces at 0º and 60º to be plotted (black trace) and fitted with a two-state model (red trace). **e)** Line scanning kymographs (top), and example model kymographs of rotations between the two preferred orientations (bottom). **f)** Distribution of dwell-times spent in each orientation before rotation, with overlaid normalized survival plots obtained by HS-AFM-HS (upper panel) and line scanning (lower panel). Histograms each contain data from 3 different trimers each showing no significant statistical differences between molecules. **g)** Histogram of the height differences obtained by subtracting height/time traces at 0º and 60º in (d). **h)** Rotation time histogram (n=22) of single resolved 60º clockwise and counter-clockwise rotations in (e).
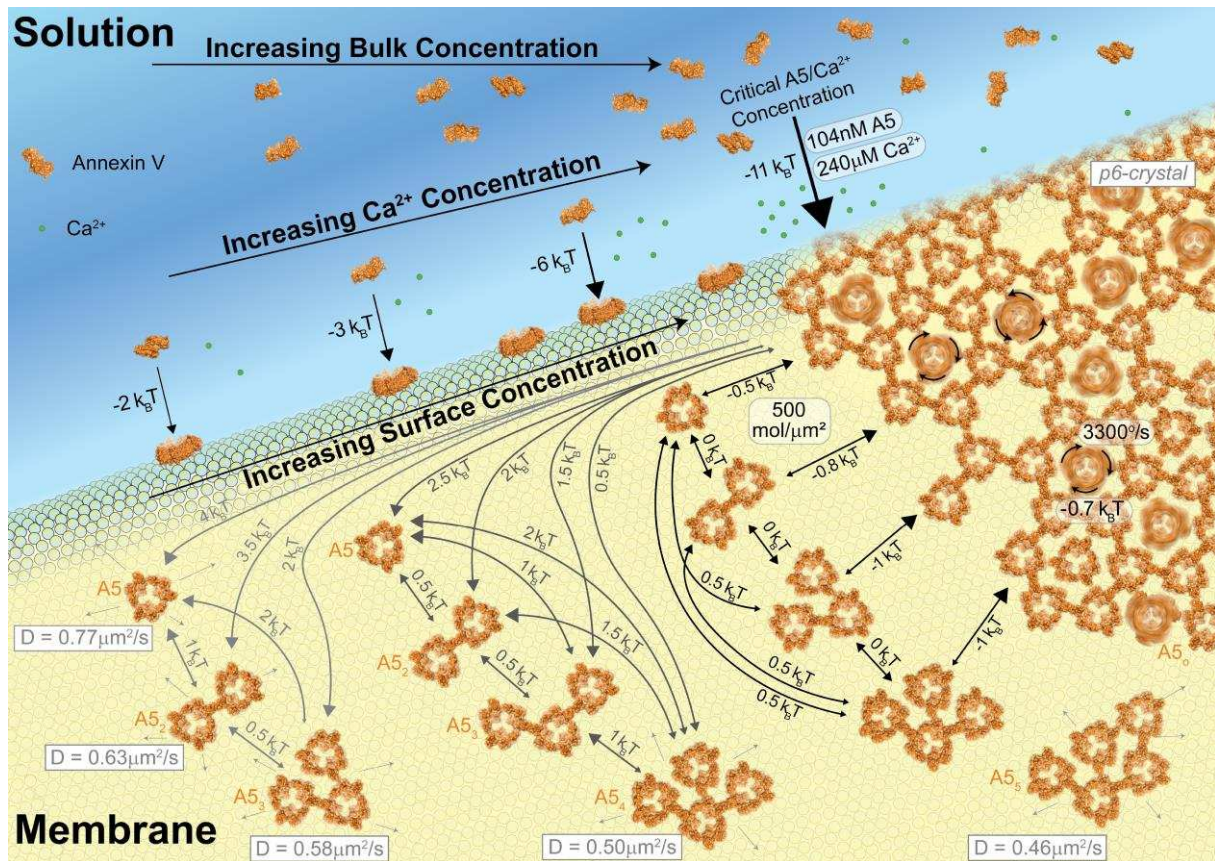
19

Figure 6) Full quantitative description of annexin-V membrane association and self-assembly. Energetic and dynamic terms of the process could be determined by HS-AFM-HS, combined with HS-AFM imaging and line scanning. The Annotated illustration describes how soluble annexin-V bind to membrane in the presence of Ca^{2+} and there, as the result of 2D diffusion, association, and crowding reach a critical 2D concentration necessary for the formation of 2D-latiices that have essentially no off-rate and thus stabilize the membrane around damages.

K_d (µm^{-2})	Monomer	Dimer	Trimer	Tetramer
Monomer	220 ± 40	170 ± 20	650 ± 60	200 ± 10
Dimer	152 ± 31	444 ± 60	210 ± 20	128 ± 8
Trimer	260 ± 50	210 ± 20	180 ± 20	109 ± 10
Tetramer	170 ± 30	106 ± 21	91 ± 18	52 ± 10

Table 1. K_d values arranged in a matrix where each molecular species arises from the sum of the components parts. K_d values were obtained by fits to equation 5 (**Supplementary Fig. 6**) (± 95% CI). K_d values for forming complexes larger than 5 units such as the tetramer-tetramer interaction, have reduced reliability as all molecular aggregates above n = 4 are taken together in the fitting.